Photonic metacrystal: Design methodology and experimental characterization

S. Hu,[1,3] M. Khater,[2,*] E. Kratschmer,[2] S. Engelmann,[2] W. M. J. Green,[2] S. M. Weiss[1,4]

[1]*Department of Electrical Engineering and Computer Science, Vanderbilt University, Nashville, Tennessee 37235, USA.*
[2]*IBM T J Watson Center, 1101 Kitchawan Road, Yorktown Heights, New York 10598, USA.*
**Current affiliation: INanoBio Inc, 1600 Adams Drive, Menlo Park, CA 94025, USA.*
[3]*shuren.hu@vanderbilt.edu*
[4]*sharon.weiss@vanderbilt.edu*

Abstract: We report a design methodology for creating high-performance photonic crystals with arbitrary geometric shapes. This design approach enables the inclusion of subwavelength shapes into the photonic crystal unit cell, synergistically combining metamaterials concepts with on-chip guided-wave photonics. Accordingly, we use the term "*photonic metacrystal*" to describe this class of photonic structures. Photonic metacrystals exploiting three different design freedoms are demonstrated experimentally. With these additional degrees of freedom in the design space, photonic metacrystals enable added control of light-matter interactions and hold the promise of significantly increasing temporal confinement in all-dielectric metamaterials.

1. Introduction

Resonances in photonic structures have been exploited for applications ranging from laser cavities [1–2] and on-chip modulators [3–5] to ultra-sensitive biosensors [6–10]. Many different types of resonances can be supported in photonic systems, including surface plasmon resonances [2, 11–16], Fano resonances [13, 17, 18], and optical cavity resonances in photonic crystals [19–26], ring resonators [3, 5–7, 10, 26, 27], and Fabry-Perot resonators [26, 28, 29]. In general, the formation of a resonant mode can be understood as a two-step process: (1) temporally confine photons in the designed structure and (2) spatially redistribute the trapped electromagnetic waves according to boundary conditions. These two steps are independent of each other. Different photonic structures use different mechanisms to achieve the first step of temporal confinement. Plasmonic resonators, such as bowties and metallic metamaterials, temporally confine photons based on the surface plasmon resonance while photonic crystals temporally confine photons based on the photonic bandgap. One key difference in the temporal confinement of these two photonic platforms is the losses: surface plasmons are very lossy due to the high absorption coefficient in metal materials [30, 31] while photonic crystals have low losses and can support high quality (Q) factors above 10^4. Although significant progress has been made in replacing metal with dielectric materials in metamaterial structures to reduce losses [30–32], all-dielectric metamaterials intrinsically lack an effective mechanism for enabling temporal confinement and therefore do not exhibit high Q-factors even when absorption losses are low [33–35]. Hence, the possibility of combining the desirable attributes of low loss, high Q-factor photonic crystals with the unique light-matter interactions achievable with metamaterials is of great interest to expanding the capabilities of photonic systems. In addition, bringing the control of amplitude and phase achievable in metamaterials that are utilized for out-of-plane applications to photonic crystals would enable new design freedoms and capabilities for on-chip, guided-wave photonics. In order to combine the best properties of

metamaterials and photonic crystals, subwavelength geometries must be integrated with photonic crystal with sufficient periodicity maintained to allow temporal confinement based on the photonic bandgap. For example, by introducing a subwavelength periodic variation in a hyperbolic medium, one can design a photonic hypercrystal with a unique photonic band structure and light-matter interactions [36, 37]. The design of hypercrystals typically leverage one-dimensional multilayer stacking of materials to achieve the necessary subwavelength periodicity. In this work, we take a different approach and instead introduce deep-subwavelength-sized features inside the unit cells of traditional photonic crystals without a requirement for utilizing a hyperbolic material. We have previously experimentally demonstrated it is possible to use photonic bandgap confinement as the first order confinement mechanism and subwavelength geometries consistent with metamaterial designs (e.g., bowtie shape) inside the photonic crystal unit cell as the second step in modal confinement to achieve extreme light concentration on par with plasmonic resonators [23, 25]. However, an in-depth investigation of the broader design methodology involved in adding metamaterial-like geometries to photonic crystals, including many new degrees of design freedom that are enabled, has not been carried out. In this work, we present an extended study of the design methodology with new experimental results.

Here, we use the name *photonic metacrystal* for structures that combine the concepts and design attributes of both metamaterials and photonic crystals. Traditional photonic crystal theory is built on the Bloch theorem, which operates at the length scale of the optical wavelength. Photonic crystal unit cells are typically made of highly symmetric geometric shapes (e.g., circles or rectangles), exclusive of any subwavelength features. We demonstrate that it is beneficial to study subwavelength features in photonic crystal unit cells for additional control of light-matter interactions. In fact, according to Bloch theorem, any geometric shape can be designed as part of a unit cell inside a photonic crystal. In addition to differences in the unit cell shape compared to traditional photonic crystals, photonic metacrystals must operate in the air band (i.e., higher frequency band above the bandgap) while traditional photonic crystals typically operate in the dielectric band (i.e., fundamental lower frequency band below the bandgap). In the air band, the electromagnetic energy is primarily confined within the void region (e.g., air holes), which leaves open the opportunity to add subwavelength dielectric inclusions that can be used to tune both the mode distribution and the band structure. This is not the case for operation in the dielectric band when the dielectric mode is concentrated in the higher dielectric constant material comprising the photonic crystal; it is not practical to insert additional design features beyond a narrow air slot in the dielectric region to modify the modal distribution because the features become too small to fabricate [24, 38]. Importantly, the additional degrees of design freedom afforded by utilizing the air band and subwavelength dielectric features in the unit cell – either by adding subwavelength dielectric shapes into a traditional circular or rectangular air hole or by altering the overall unit cell shape – enable an interesting interplay between the polarization of light propagating in the photonic metacrystal and electromagnetic boundary conditions. For example, for transverse electric (TE) polarization, light is localized in air slots oriented along the direction of propagation and dielectric bars (i.e., antislots) oriented orthogonal to the direction of propagation through the slot and antislot effects [23, 25]. These air slots and dielectric antislots can also be used as building blocks for localizing light in more complicated subwavelength features such as bowties and other shapes used in metamaterials design [23, 25]. In the following sections, we discuss simulations that demonstrate the feasibility of designing a photonic metacrystal with an arbitrary shaped “cat-paw” unit cell and show experimental results for silicon photonic metacrystals exploiting three different design freedoms: radius modulated bowtie-shaped unit cell, rotation angle modulated bowtie-shaped unit cell, and bowtie connection width modulated bowtie-shaped unit cell. The latter two design freedoms are not available in traditional photonic crystals.

2. Photonic metacrystal and its design methodology

To build our intuition on the band structure of the photonic metacrystal, we first analyze the guiding mode in a traditional waveguide. Shown in **Figure 1A** is a photonic band diagram of a one-dimensional (1D) waveguide mode. Due to the translational invariance, modes 1 and 2 are degenerate modes of the waveguide, with a spatial phase difference of π, that correspond to the same mode in the band diagram. To break the translational invariance, we consider superimposing an array of repetitive air holes with arbitrary shapes, e.g., cat paw, on the waveguiding modes 1 and 2. Mode 1 becomes the "dielectric mode" for which most optical field intensity is located within the dielectric region between the air holes. Mode 2 becomes the "air mode" for which the maximum field intensity spatially overlaps with the air holes. These two types of modal overlaps give different energy perturbations and result in a mode split at the edge of the Brillouin zone in the photonic band diagram. The opening of this mode split is the photonic bandgap, within which light is not allowed to propagate, as shown in **Figure 1 B**.

As demonstrated by the cat paw cavity, a high Q photonic crystal can be designed using arbitrary geometrical shapes (**Figure 1 C and D**). Building on this concept, we propose a photonic metacrystal design methodology that focuses on engineering the shape of the unit cells. While the "cat paw" photonic crystal illustrates an extreme example of unit cell design freedom, **Figure 2 A-C** shows more practical examples of photonic metacrystal unit cells created by adding a dielectric nanowire (300×50 nm) or bowtie shaped nanoparticle to a circular unit cell. Such nanowire and bowtie shapes have been extensively studied as plasmonic elements and metamaterial building blocks [11–16, 18, 33–35]. A key aspect of the photonic metacrystal design is to utilize the air mode. The air mode traps light within the open area of the unit cell, which provides an ideal platform for inserting subwavelength scatterers of interest. The simulated electric field and electric energy mode profiles (air mode at band edge k_x=0.5) for TE-polarized light in **Figure 2 D** and **E** show the uniformly distributed electric field within the air hole of the circular unit cell and how inserting subwavelength nanoparticles into that unit cell can deterministically modify the mode profiles. The modified mode profile results from redistribution of the electric and displacement fields based on boundary conditions [23–25]. **Table 1** provides a summary of comparisons between traditional photonic crystal and photonic metacrystal design.

In the air mode, the optical field can be strongly perturbed by the presence of nanoparticles included in the air holes. Importantly, not only the shape but also the placement (e.g., rotational angle) of the nanoparticles affects the field profile. For example, as shown in **Figure 2 D** and **E**, due to electromagnetic boundary conditions, the antislot R0 unit cell exhibits the minimum electric field inside the dielectric nanowire, while the antislot R90 unit cell exhibits a nearly uniform electric field intensity in the dielectric nanowire and surrounding air region of the unit cell. Due to the discontinuity of the displacement field inside the antislot R90 unit cell, the majority of the electric energy resides inside the dielectric nanowire while minimal electric energy resides inside the nanowire in the antislot R0 unit cell. The bowtie unit cell shows even more drastic changes in the electric field and electric energy distribution between R0 and R90 cases. In the R0 bowtie unit cell, most of the electric field is distributed in the air region. However, in the R90 bowtie unit cell, the electric field is highly concentrated at the bowtie tips. These trends are accentuated even more when comparing the electric energy distributions of the R0 and R90 bowtie unit cells. This ability to engineer the mode profile of the air-mode photonic crystal with strategically shaped and oriented dielectric nanoparticle inclusions (i.e., the photonic metacrystal) opens the door to studying light-matter interactions under extremely high Q factor regimes using in-plane guided waves with modest input light intensity.

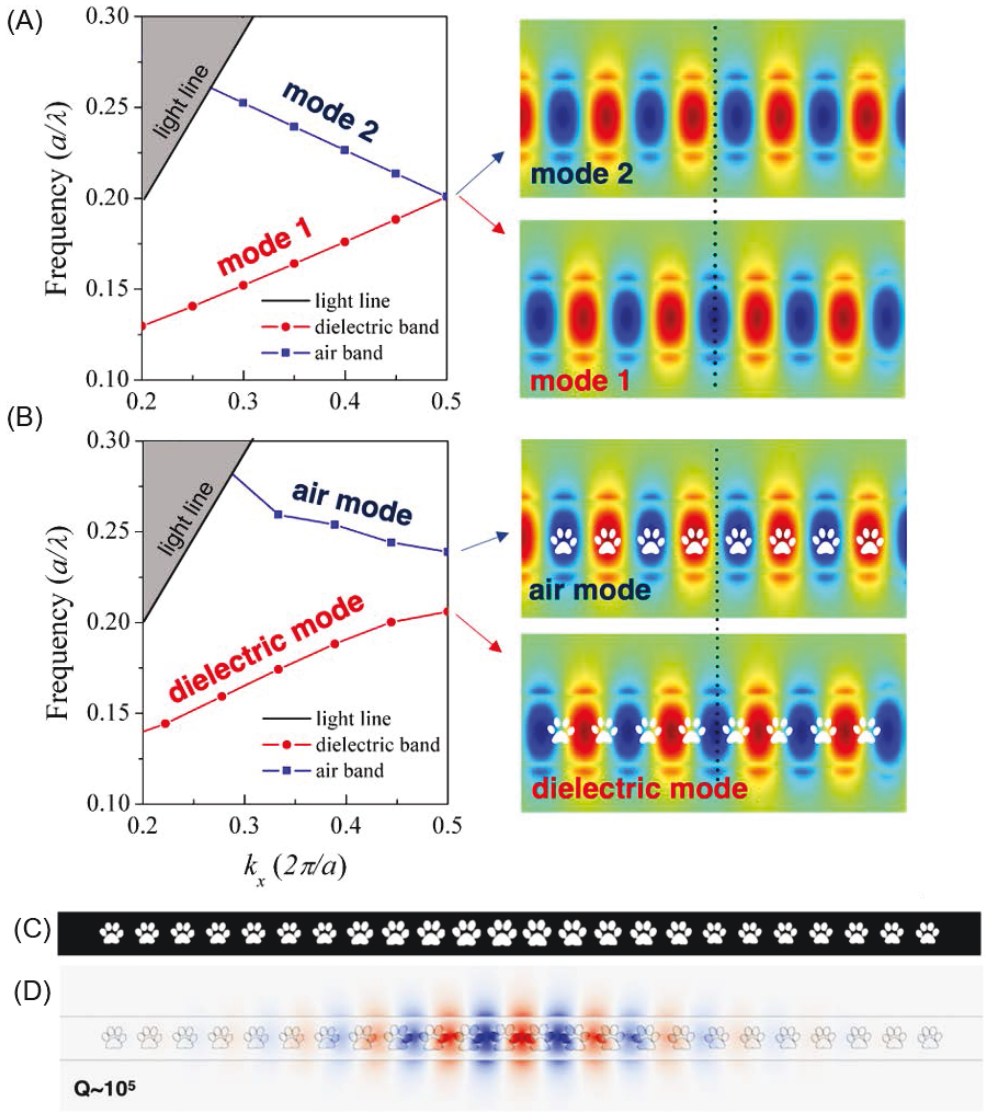

Figure 1. 1D photonic crystal and its bandgap formation from the guided mode. (A) Photonic band structure and electric field profile of degenerated waveguide mode (mode 1 and 2) with a spatial phase difference of π. (B) Photonic band structure and conceptual illustration showing cat paw PhC unit cells superimposed on the electric field profiles for waveguided mode 1 and 2, revealing the origin of the distinct air and dielectric band edge modes. (C) Schematic of 1D cat paw photonic crystal with three mirror unit cells and nine taper unit cells. (D) 3D FDTD simulated dielectric mode profile of cat paw photonic crystal with Q ~ 10^5.

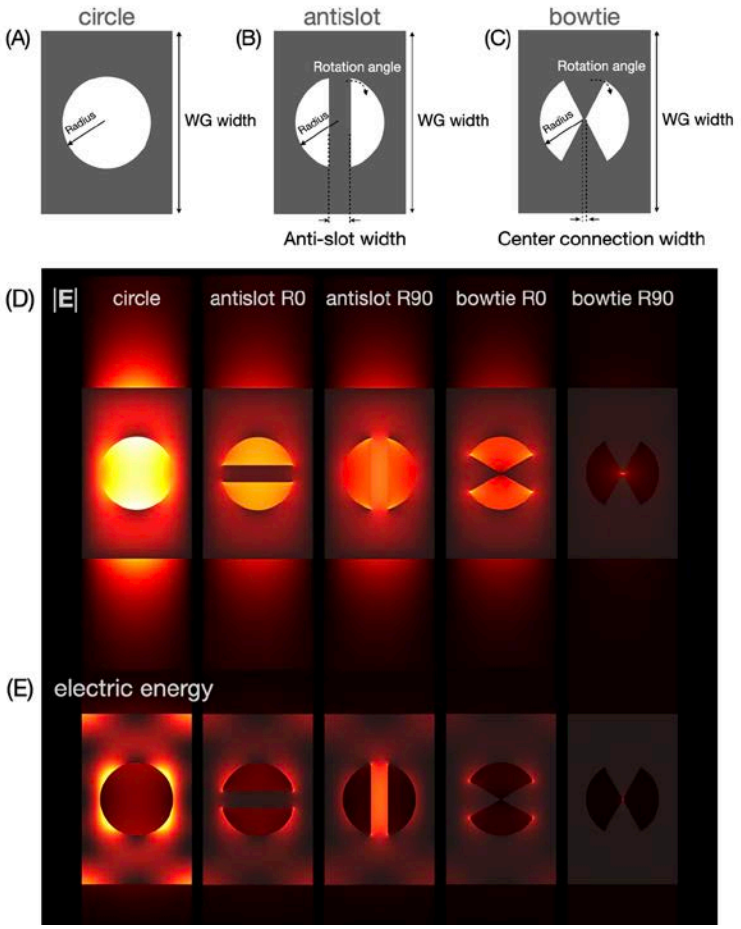

Figure 2. Examples of different unit cells in photonic metacrystal designs. Design degrees of freedom in a (A) typical circle, (B) antislot, and (C) bowtie unit cell. (D) and (E) show simulated mode distribution of electric field and electric energy, respectively, in different unit cells.

Table 1. Comparison between traditional photonic crystals and photonic metacrystals

	Traditional photonic crystal	**Photonic metacrystal**
Unit cell	Highly symmetric shape (e.g., circles, squares, and rectangles)	Any geometric shape
Mode	Dielectric mode (lower frequency below the bandgap)	Air mode (higher frequency above the bandgap)
Design focus	Improve Q-factor	Interaction between subwavelength scatterers and light while maintaining a high Q-factor
Design parameters	Periodicity and filling factors	Any degree of freedom within the unit cell, such as rotation angle and other dimension changes

In the following section, we take the bowtie unit cell as an example of a photonic metacrystal unit cell and explore new approaches to cavity design enabled by new degrees of freedom in the unit cell. As illustrated in **Figure 2 A-C**, the degrees of freedom in a traditional circular unit cell include only radius and waveguide width. By adding a rectangular dielectric nanowire (i.e., antislot), two more degrees of freedom are enabled: rotational angle of the antislot and antislot width. With a bowtie shaped dielectric block inside the air hole, even more

degrees of freedom are enabled, including the bowtie tip angle, bowtie connection width, and bowtie rotation angle.

3. Bowtie photonic metacrystal design and experimental results

The bowtie photonic metacrystals presented in this section are designed to have in-line coupling between the bus waveguide (*i.e.,* ridge waveguide with no air holes) and photonic metacrystal cavities. For this coupling configuration, photons at the resonance frequencies tunnel through the mirror segments of the photonic metacrystal and evanescently couple into the cavity. The coupling coefficient between the waveguide and cavity is determined in large part by the mirror strength of the photonic metacrystal unit cells. The total mirror strength can be controlled by two design parameters: the mirror strength of each mirror unit cell and the number of mirror unit cells. Regarding the strength of each mirror unit cell, we refer to the mirror strength calculation discussed in Refs. 21–22. There are two key parameters for mirror strength: the size of the photonic band gap and the frequency span between the resonance frequency and midgap frequency. The mirror strength of a single unit cell is strongest when 1) the size of the band gap is maximized and 2) the resonance frequency is located in the middle of the band gap. There are other coupling configurations, such as side-coupling, that can achieve similar or potentially improved performance without the trade-off between Q and transmission [39].

3.1 Bowtie photonic metacrystal cavities designed by radius modulation

Figure 3 shows silicon bowtie photonic metacrystals designed following a traditional method of modulating the filling factor of the unit cells (i.e., the size of the air holes). The cavity is formed with 450 nm constant periodicity, 700 nm waveguide width, a center unit cell of 150 nm radius and mirror unit cells of 187 nm radii on both sides. The air hole size is gradually tapered from the center to the mirror segments. Design details including the choice of photonic crystal dimensions and FDTD boundary conditions are discussed in Ref. 23 and 25. **Figure 3 A-B** shows SEM images of one of the fabricated devices using standard electron beam lithography (EBL) and reactive ion etching processes. The bowtie connection is accurately formed by the EBL process. The photonic metacrystals were fabricated on 8-inch silicon-on-insulator wafers with a 220 nm device layer and 2 μm-thick buried oxide layer (Soitec). Detailed fabrication process information is included in Ref. 25.

Figure 3 C-K shows the measurement results with different numbers of mirror segments. All transmission measurements reported in this work were carried out using our polarization maintained optical fiber coupling setup with piezo-controlled XYZ stages. A tunable continuous-wave laser (Stantec TSL-510) was used to perform passive transmission measurements, using quasi-TE polarization, over the wavelength range of 1500 to 1630 nm. Transmitted optical power was measured by a near infrared photodetector. The expected tradeoff between the peak transmission and Q factor is evident with higher Q resonances having lower transmission intensity. **Figure 3 C-E** shows the results from a device with 10 taper unit cells from the cavity center to the mirror and 5 additional mirror unit cells on each side. The transmission spectrum is normalized to its highest peak at the band edge. For the fundamental mode, the normalized transmission is 0.6 and Q factor is near 3,000. As the number of mirror segments is increased to 8 unit cells on each side, the normalized transmission of the fundamental mode decreases to 0.2 while the Q factor increases to ~ 11,000 (**Figure 3 F-H**). Finally, when the number of mirror segments is increased to 11 unit cells on each side, the normalized transmission is only 0.08 but the Q factor is increased to ~ 16,000 (**Figure 3 I-K**). We note that the measured resonances are close to the air band edge, unlike the case for traditional photonic crystal resonators that are designed for dielectric modes. Due to fabrication variations, the absolute resonance wavelengths are likely to vary between devices. However, since the tapering profiles are the same among these three devices, the distance between resonance and band edge (2^{nd} mode) wavelength remains the same, as shown in Figure 3 C, G and J.

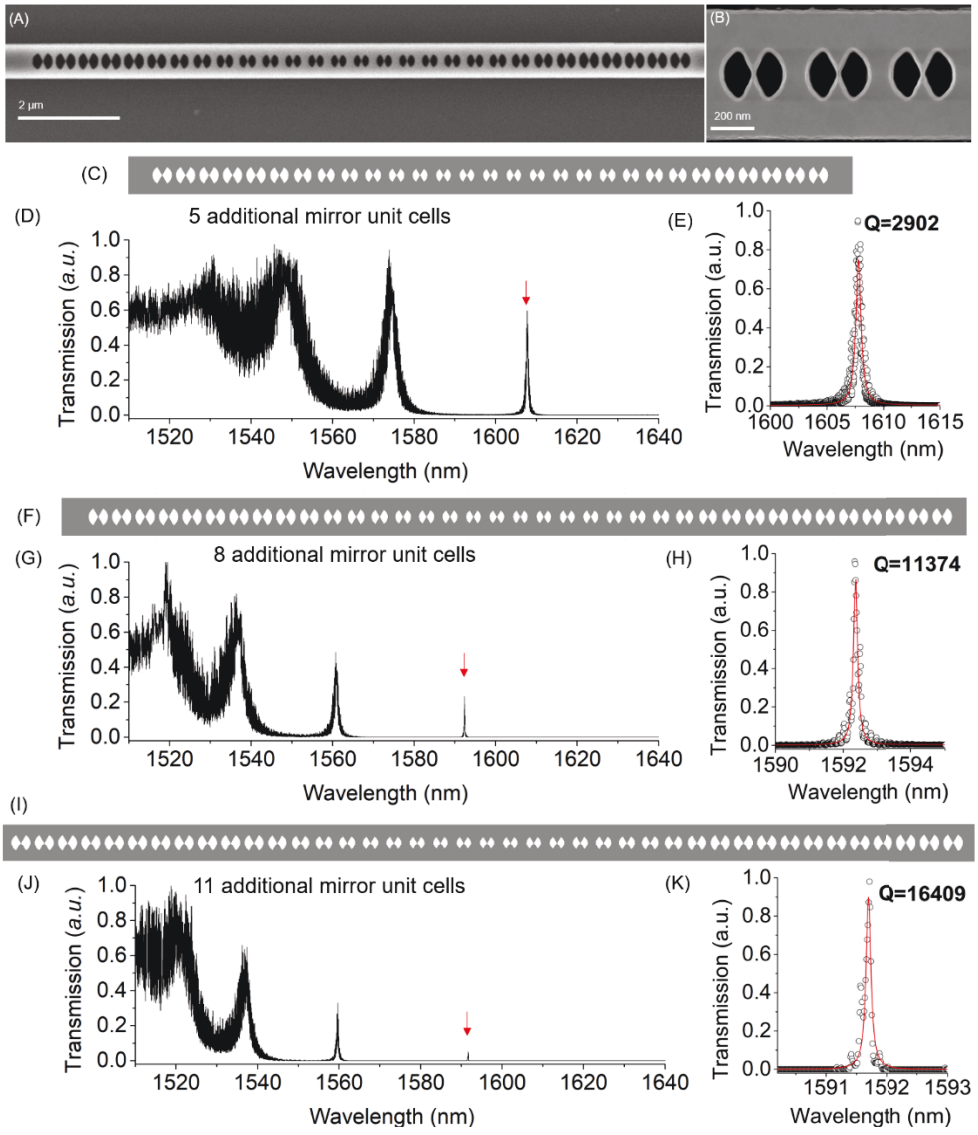

Figure 3. Silicon bowtie photonic metacrystal designed with radius modulation. (A) SEM image of fabricated device. (B) Zoom-in SEM of three mirror unit cells. (C) Schematic and (D-E) measured transmission of a radius modulated bowtie photonic metacrystal designed with 5 mirror unit cells and 10 taper unit cells. (F) Schematic and (G-H) measured transmission of a radius modulated bowtie photonic metacrystal designed with 8 mirror unit cells and 10 taper unit cells. (I) Schematic and (J-K) measured transmission of a radius modulated bowtie photonic metacrystal designed with 11 mirror unit cells and 10 taper unit cells.

3.2 Bowtie photonic metacrystal cavities designed by rotation angle modulation

When a subwavelength dielectric feature is added to the air hole unit cell, the rotational symmetry of the unit cell is broken. This rotational degree of freedom can be utilized to design a unique rotational photonic metacrystal cavity. As shown in the **Figure 4**, the band edge frequency of the air band decreases as the rotation angle increases from 0° to 90° (i.e., from the R0 unit cell to the R90 unit cell). Here R0 means the bowtie is oriented parallel to the propagation direction of light and R90 means that the bowtie is oriented orthogonal to the propagation direction. The reduction in air band edge frequency is due to the antislot effect and relative change in the field distribution in the unit cell, as discussed in detail in Refs. 23 and 25.

Because the R90 band edge frequency lies within the bandgap of the R0 unit cell, it is possible to design a photonic metacrystal resonator with an R90 unit cell at the center of the cavity and R0, or other low rotation angle unit cells at both ends, serving as mirror unit cells. The mirror strength of the R0 unit cell is the strongest because it has the largest band gap, as shown in **Figure 4**. The confinement strength of each individual unit cell can be continuously adjusted by tuning the rotation angle.

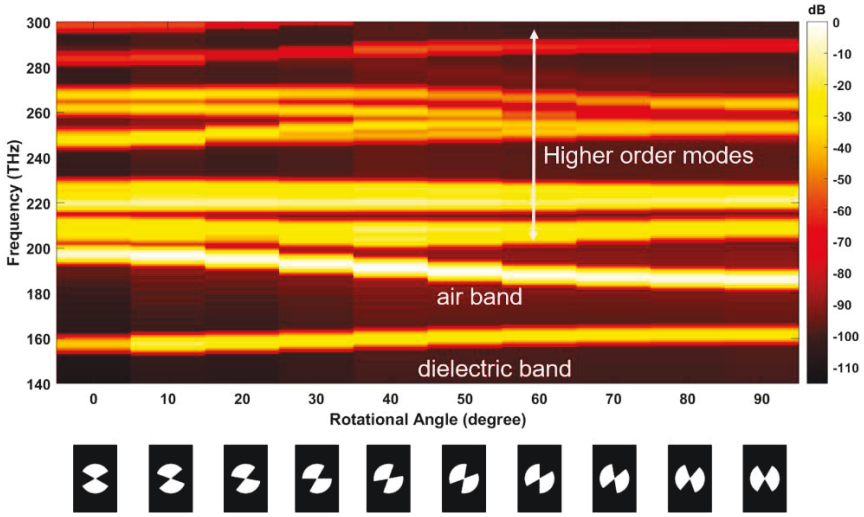

Figure 4. Photonic band edge frequency change as a function of bowtie rotation angle. The color map represents the transmission intensity with brighter yellow indicating higher transmission and darker red indicating low or no transmission.

Figure 5 shows the first reported experimental results on the rotational silicon bowtie photonic metacrystal cavity, following our earlier design work [23]. The SEM images in **Figure 5 A and B** show that the center bowtie is well resolved after fabrication and all bowties maintain a consistent shape through the different rotation angles. **Figure 5 C-H** shows transmission measurements of two cavities designed with R0 or R15 as the mirror unit cell. Both cavities are designed with 150 nm radius, 700 nm waveguide width, 400 nm constant periodicity, and tapered at 5°/step. The cavity designed using R0 as the mirror unit cell has higher Q factor ~ 51,000, but lower transmission ~ 0.03. In comparison, the cavity designed with R15 as the mirror unit cell has lower Q factor ~ 10,000 and higher transmission ~ 0.2. This result is consistent with the band diagram (**Figure 4**) that indicates that the R15 unit cell has lower mirror strength than the R0 unit cell.

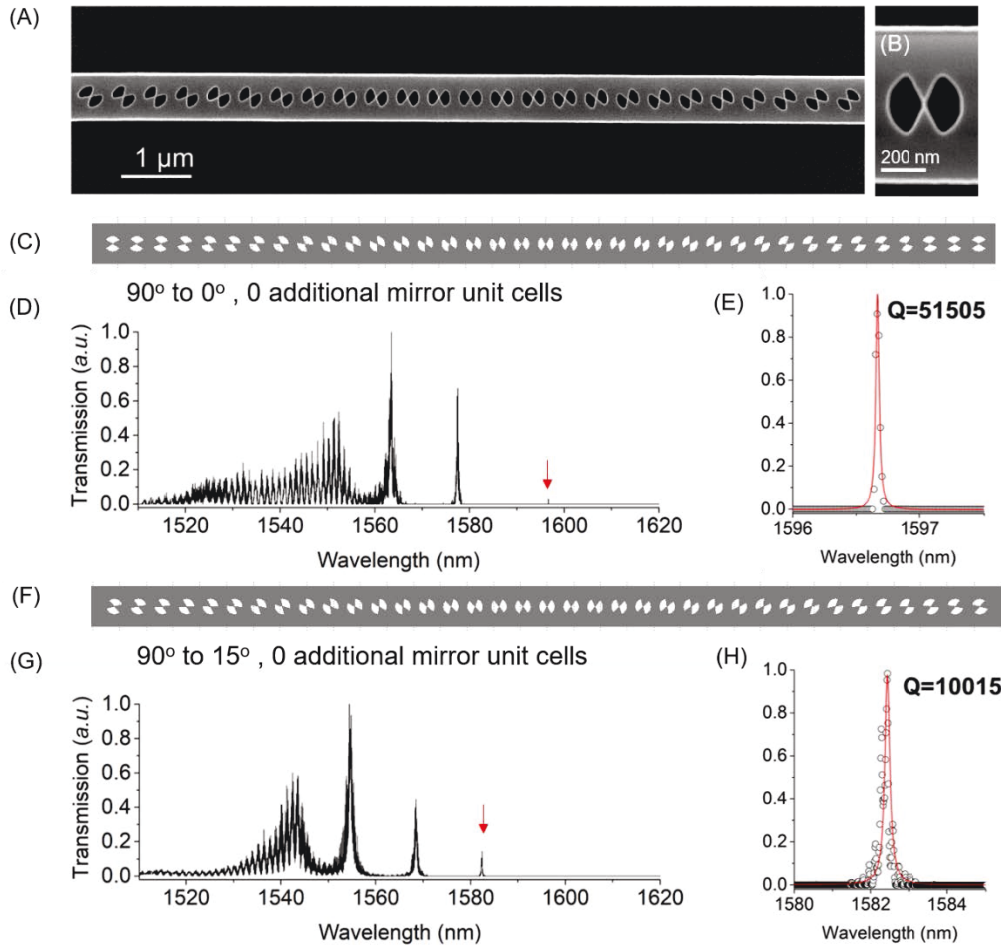

Figure 5. Silicon bowtie photonic metacrystal designed by modifying the rotation angle of the bowtie unit cell. (A) SEM image of fabricated device. (B) Zoom-in SEM of center cavity R90 unit cell. (C) Schematic and (D-E) measured transmission of a rotation angle modulated bowtie photonic metacrystal designed with R0 as mirror unit cell. (F) Schematic and (G-H) measured transmission of a rotation angle modulated bowtie photonic metacrystal designed with R15 as mirror unit cell. Both cavities in (C) and (F) are designed to have 5^{o}/step tapering from the center (90^{o}) to the mirror unit cells (0^{o} or 15^{o}).

3.3 Bowtie photonic metacrystal cavities designed by bowtie tip connection width modulation

While an ideal bowtie shape has very sharp tips with a connection width approaching zero, fabrication limitations require a finite connection width of size dictated by the fabrication approach utilized. Here we demonstrate that using the bowtie connection width as a tunable parameter can enable another unique approach to designing a photonic metacrystal. Because the optical energy is highly confined in the bowtie tip connection region (e.g., see the mode profile in **Figure 2)**, the light-matter interaction is strongest at this location. As a result, the photonic band structure is strongly influenced by refractive index perturbations in this center connection region.

The photonic band edge frequency change as a function of bowtie connection width is shown in **Figure 6**. Similar to the rotational design case (**Figure 4**), the dielectric band edge frequency remains nearly constant, but the air band edge frequency has a strong dependence on the connection width. By changing the connection width from 0 to 100 nm, where a 100 nm

connection width essentially converts the bowtie to an antislot shape, the air band frequency drops from 190.7 THz to 160.8 THz, corresponding to a wavelength change from 1573 nm to 1866 nm. It is interesting to note that the silicon volume change corresponding to the geometry change from a 0 to 100 nm connection width is only 1.9×10^6 nm^3, which is equivalent to a silicon mass change of ~ 4.4 femtogram. Remarkably, these values reveal a spectral sensitivity of ~ 66 nm per femtogram of silicon mass change. This extreme spectral sensitivity can be an advantage or challenge depending on the application. For example, the bowtie photonic crystal could be employed as an ultrasensitive biosensor, assuming molecules would be guided to the bowtie connection tip through clever flow geometries and with the assistance of the optical gradient force that results from the strong gradient in energy density in the tip region [40]. However, for applications that rely on reproducibly fabricating devices at a precise resonance wavelength, resistive heaters or other active approaches would likely be required to fine tune the resonance position.

Figure 7 A - D shows SEM images of a fabricated silicon bowtie connection width modulated photonic metacrystal. This cavity was designed by linearly changing the connection width from 60 nm to 0 nm with a 5 nm/step tapering profile. The width of the nanobeam is 700 nm, the diameter of the air holes is 300 nm, and the period is 450 nm. The device shown in **Figure 7** was suspended using a standard photolithography and buffered oxide etch undercut process to remove the supporting oxide layer. Detailed process steps are discussed in Ref. 10. The 0 nm bowtie connection width design turned out to be ~ 5 nm after fabrication. The device performance can be improved further by optimizing the tapering profile in the design following the actual process limitations. **Figure 7 E – G** shows the measured transmission spectra for cavity designs with different numbers of additional mirror unit cells (0, 3 and 9). Similar to the trends discussed previously, the photonic metacrystal cavities with fewer additional mirror unit cells have a lower Q but higher peak transmission of the fundamental mode. Accordingly, the highest transmission and lowest Q ~ 5000 occurs for the bowtie connection width modulated photonic metacrystal with no additional mirror unit cells (**Figure 7E**). As number of additional mirror unit cells increases to 3, the Q increases to ~ 50,000 but the transmission decreases (**Figure 7F**). For the bowtie connection width modulated photonic metacrystal with 9 additional mirror unit cells, the fundamental peak is below our measurement noise and can no longer be resolved (**Figure 7G**).

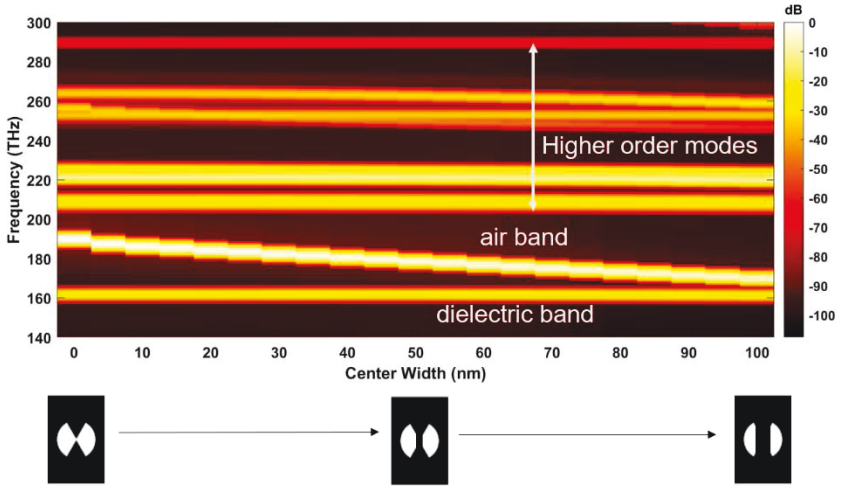

Figure 6. Photonic band edge frequency change as a function of bowtie connection width. The color map represents the transmission intensity in dB with brighter yellow indicating higher transmission and darker red indicating low or no transmission.

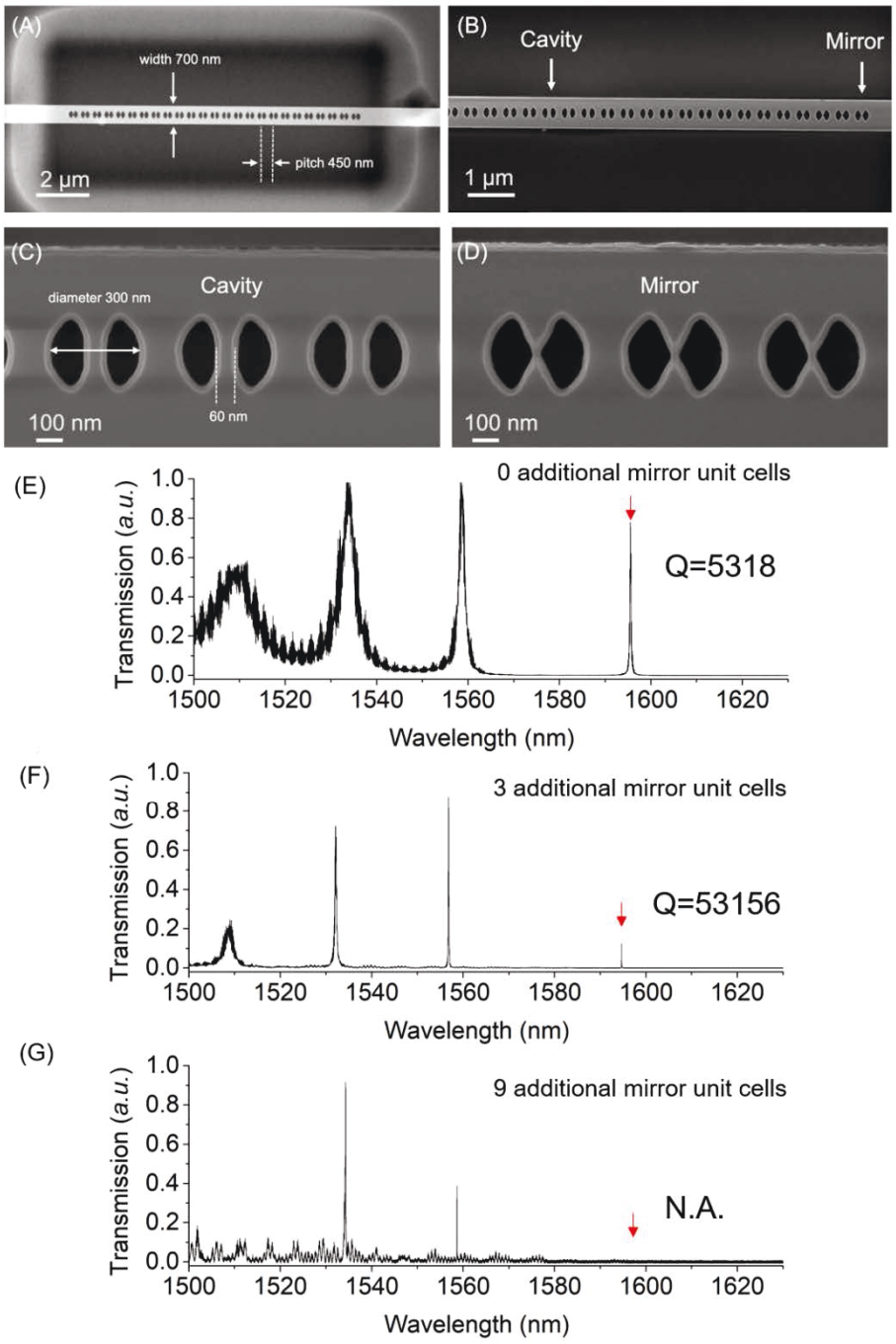

Figure 7. (A-D) SEM images of a suspended, connection-width modulated silicon bowtie photonic metacrystal cavity. The connection width of the cavity center unit cell is 60 nm and tapers to a connection width approaching zero for the mirrors. (E-G) Measured transmission spectra of cavities with 0, 3 and 9 additional mirror unit cells shown with the fundamental resonance near 1594.7 nm.

4. Conclusion

We described a class of photonic crystal – the *photonic metacrystal* – that combines the advantages of photonic crystals and metamaterials by introducing subwavelength scatterers into the photonic crystal unit cell. With the requirement of operation in the air mode, light-matter

interaction can be tailored through the deterministic design of the subwavelength dielectric features inside the air holes of the photonic metacrystal. We experimentally demonstrated that new unit cell design features, including the rotation angle and connection width of a bowtie-shaped unit cell, can be modified to predictably tune the optical band structure and create high Q cavities. These additional degrees of freedom, which are not present in traditional photonic crystals, provide new ways to simultaneously control the band structure in *k* space and the mode profile in real space. We believe the continued investigation and utilization of photonic metacrystals will significantly expand the application space of guided wave photonics, leading to breakthroughs with quantum emitters, spin-orbit coupling, topological optics and optical sensing.

Funding. National Science Foundation (ECCS1407777; ECCS1809937).

Acknowledgments. This work was supported in part by the National Science Foundation (ECCS1407777; ECCS1809937). The photonic metacrystal cavities were fabricated in the Microelectronics Research Laboratory (MRL) at the IBM Thomas J. Watson Research Center. The authors are grateful to the MRL staff for their contributions to the success of this work. Simulations presented in this work were conducted in part using the resources of the Advanced Computing Center for Research and Education at Vanderbilt University.

Disclosures. The authors declare no conflicts of interest.

Data availability. Data underlying the results presented in this paper are not publicly available at this time but may be obtained from the authors upon reasonable request.

References

1. S. Noda, M. Fujita, and T. Asano, "Spontaneous-emission control by photonic crystals and nanocavities," Nat. Photon. **1**(8), 449–458 (2008).
2. R. F. Oulton, V. J. Sorger, T. Zentgraf, R. Ma, C. Gladden, L. Dai, G. Bartal, and X. Zhang, "Plasmon lasers at deep subwavelength scale," Nature **461**(7264), 629–632 (2009).
3. Q. Xu, B. Schmidt, S. Pradhan, and M. Lipson, "Micrometre-scale silicon electro-optic modulator," Nature **435**(7040), 325–327 (2005).
4. G. T. Reed, G. M.ashanovich, F. Y. Gardes, and D. J. Thomson, "Silicon optical modulators," Nat. Photon. **4**(8), 518–526 (2010).
5. J. C. Rosenberg, W. M. Green, S. Assefa, D. M. Gill, T. Barwicz, M. Yang, S. M. Shank, and Y. A. Vlasov, "A 25 Gbps silicon microring modulator based on an interleaved junction," Opt. Express **20**(24), 26411 (2012).
6. M. Iqbal, M. A. Gleeson, B. Spaugh, F. Tybor, W. G. Gunn, M. Hochberg, T. Baehr-Jones, R. C. Bailey, and L. C. Gunn, "Label-free biosensor arrays based on silicon ring resonators and high-speed optical scanning instrumentation," IEEE J. Sel. Top. Quantum Electron. **16**(3), 654–661 (2010).
7. F. Vollmer and L. Yang, "Review label-free detection with high-Q microcavities: a review of biosensing mechanisms for integrated devices," Nanophotonics **1**(3–4), 267–291 (2012).
8. S. Chakravarty, W. Lai, Y. Zou, H. A. Drabkin, R. M. Gemmill, G. R. Simon, S. H. Chin, and R. T. Chen, "Multiplexed specific label-free detection of NCI-H358 lung cancer cell line lysates with silicon based photonic crystal microcavity biosensors," Biosens. Bioelectron. **43**(15), 50–55 (2013).
9. S. Hu, Y. Zhao, K. Qin, S. T. Retterer, I. I. Kravchenko, and S. M. Weiss, "Enhancing the sensitivity of label-free silicon photonic biosensors through increased probe molecule density," ACS Photon. **1**(7), 590–597 (2014).
10. G. Gaur, S. Hu, R. L. Mernaugh, I. I. Kravchenko, S. T. Retterer, and S. M. Weiss, "Label-free detection of Herceptin using suspended silicon microring resonators," Sens. Act. B **275**(1), 394–401 (2018).
11. H. Fischer and O. J. F. Martin, "Engineering the optical response of plasmonic nanoantennas," Opt. Express **16**(12), 9144–9154 (2008).
12. J. A. Schuller, E. S. Barnard, W. Cai, Y. C. Jun, J. S. White, and M. L. Brongersma, "Plasmonics for extreme light concentration and manipulation," Nat. Mater. **9**(3), 193–204 (2010).
13. B. Luk'Yanchuk, N. I. Zheludev, S. A. Maier, N. J. Halas, P. Nordlander, H. Giessen, and C. T. Chong, "The Fano resonance in plasmonic nanostructures and metamaterials," Nat. Mater. **9**(9), 707–715 (2010).
14. D. K. Gramotnev, A. Pors, M. Willatzen, and S. I. Bozhevolnyi, "Gap-plasmon nanoantennas and bowtie resonators," Phys. Rev. B. **85**(4), 045434 (2012).
15. S. Park, J. W. Hahn, and J. Y. Lee, "Doubly resonant metallic nanostructure for high conversion efficiency of second harmonic generation," Opt. Express **20**(5), 4856–4870 (2012)
16. V. Flauraud, T. S. van Zanten, M. Mivelle, C. Manzo, M. F. G. Parajo, and J. Brugger, "Large-scale arrays of bowtie nanoaperture antennas for nanoscale dynamics in living cell membranes," Nano Lett. **15**(6), 4176-4182 (2015).
17. W. Zhou, D. Zhao, Y. Shuai, H. Yang, S. Chuwongin, A. Chadha, J. Seo, K. X. Wang, V. Liu, Z. Ma, and S. Fan, "Progress in 2D photonic crystal Fano resonance photonics," Prog. Quantum Electron. **38**(1), 1–74 (2014).

18. J. Yan, P. Liu, Z. Lin, H. Wang, H. Chen, C. Wang, and G. Yang, "Directional Fano resonance in a silicon nanosphere dimer," ACS Nano **9**(3) 2968-2980 (2015).
19. Y. Akahane, T. Asano, B. Song, and S. Noda, "High-Q photonic nanocavity in a two-dimensional photonic crystal," Nature **425**(6961), 944–947 (2003).
20. B. Song, S. Noda, T. Asano, and Y. Akahane, "Ultra-high-Q photonic double-heterostructure nanocavity," Nat. Mater. **4**(3), 207–210 (2005).
21. Q. Quan, P. B. Deotare, and M. Loncar, "Photonic crystsal nanobeam cavity strongly coupled to the feeding waveguide," Appl. Phys. Lett. **96**(20), 203102 (2010).
22. Q. Quan and M. Loncar, "Deterministic design of wavelength scale, ultra-high Q photonic crystal nanobeam cavities," Opt. Express **19**(19), 18529–18542 (2011).
23. S. Hu and S. M. Weiss, "Design of photonic crystal cavities for extreme light concentration," ACS Photon. **3**(9), 1647–1653 (2016).
24. H. Choi, M. Heuck, and D. Englund, "Self-similar nanocavity design with ultrasmall mode volume for single-photon nonlinearities," Phys. Rev. Lett. **118**(22), 223605 (2017).
25. S. Hu, M. Khater, R. Salas-Montiel, E. Kratschmer, S. Engelmann, W. M. J. Green, and S. M. Weiss, "Experimental realization of deep subwavelength confinement in dielectric optical resonators," Sci. Adv. **4**(8), eaat2355 (2018).
26. K. J. Vahala, "Optical microcavities," Nature **424**(6950), 839–846 (2003).
27. W. Bogaerts, P. D. Heyn, T. V. Vaerenbergh, K. D. Vos, S. K. Selvaraja, T. Claes, P. Dumon, P. Bienstman, D. V. Thourhout, and R. Baets, "Silicon microring resonators," Laser Photon. Rev. **6**(1), 47–73 (2012).
28. M. S. Unlu and S. Strite, "Resonant cavity enhanced photonic devices," J. Appl. Phys. **78**(2), 607–639 (1995).
29. C. Hofmann, A. Gorbunov, M. Gorbunov, M. Strauss, S. Reitzenstein, C. Hofmann, A. Gorbunov, M. Strauß, S. H. Kwon, C. Schneider, A. Löffler, S. Höfling, M. Kamp, A. Forchel, "AlAs/GaAs micropillar cavities with quality factors exceeding 150.000," Appl. Phys. Lett. **90**(25), 251109 (2007).
30. J. B. Khurgin, "How to deal with the loss in plasmonics and metamaterials," Nat. Nano. **10**(1), 2-6 (2015).
31. A. Boltasseva, V. M. Shalaev, "All that glitters need not be gold," Science **347**(6228), 1308–1310 (2015).
32. P. Moitra, Y. Yang, Z. Anderson, I. I. Kravchenko, D. P. Briggs, and J. Valentine, "Realization of an all-dielectric zero-index optical metamaterial," Nat. Photonics **7**(10), 791–795 (2013).
33. Q. Lu, F. Shu, and C. Zhou, "Dielectric bow-tie nanocavity," Opt. Lett. **38**(24) 5311–5314 (2013).
34. R. M. Bakker, D. Permyakov, Y. F. Yu, D. Markovich, R. Paniagua-Dominguez, L. Gonzaga, A. Samusev, Y. Kivshar, B. Lku'yanchuk, and A. I. Kuznetsov, "Magnetic and electric hotspots with silicon nanodimers," Nano Lett. **15**(3), 2137–2142 (2015).
35. A. L. Holsteen, S. Raza, P. Fan, P. G. Kik, and M. L. Brongersma, "Purcell effect for active tuning of light scattering from semiconductor optical antennas," Science **358**(6369), 1407–1410 (2017).
36. E. E. Narimanov, "Photonic hypercrystals," Phys. Rev. X **4**(4), 041014 (2014).
37. T. Galfsky, J. Gu, E. E. Narimanov, and V. M. Menon, "Photonic hypercrystals for control of light-matter interactions," Proc. Natl. Acad. Sci. **114**(20), 5125–5129 (2017).
38. J. D. Ryckman and S. M. Weiss, "Low mode volume slotted photonic crystal single nanobeam cavity," Appl. Phys. Lett. **101**(7), 071104 (2012).
39. S. I. Halimi, S. Hu, F. O. Afzal, and S. M. Weiss, "Realizing high transmission intensity in photonic crystal nanobeams using a side-coupling waveguide," Opt. Lett. **43**(17), 4260–4263 (2018).
40. S. Yang, J. A. Allen, C. Hong, K. P. Arnold, S. M. Weiss, and J. C. Ndukaife, "Multiplexed long-range electrohydrodynamic transport and nano-optical trapping with cascaded bowtie photonic crystal cavities," arXiv:2109.14168